Constructing a pathway for mixed ion and electron transfer reactions for O_2 incorporation in $Pr_{0.1}Ce_{0.9}O_{2-x}$

Di Chen [1,6], Zixuan Guan[2], Dawei Zhang[1], Lena Trotochaud [3,7], Ethan Crumlin [4], Slavomir Nemsak[3], Hendrik Bluhm[3,8], Harry L. Tuller[5] and William C. Chueh [1*]

In interfacial charge-transfer reactions, the complexity of the reaction pathway increases with the number of charges transferred, and becomes even greater when the reaction involves both electrons (charge) and ions (mass). These so-called mixed ion and electron transfer (MIET) reactions are crucial in intercalation/insertion electrochemistry, such as that occurring in oxygen reduction/evolution electrocatalysts and lithium-ion battery electrodes. Understanding MIET reaction pathways, particularly identifying the rate-determining step (RDS), is crucial for engineering interfaces at the molecular, electronic and point defect levels. Here we develop a generalizable experimental and analysis framework for constructing the reaction pathway for the incorporation of $O_2(g)$ in $Pr_{0.1}Ce_{0.9}O_{2-x}$. We converge on four candidates for the RDS (dissociation of neutral oxygen adsorbate) out of more than 100 possibilities by measuring the current density–overpotential curves while controlling both oxygen activity in the solid and oxygen gas partial pressure, and by quantifying the chemical and electrostatic driving forces using operando ambient pressure X-ray photoelectron spectroscopy.

M ixed ion and electron transfer (MIET) reactions involve the transfer of both ionic and electronic charges across interfaces. They are substantially more complex than electron transfer and proton-coupled electron transfer reactions because the ions also cross the electrochemical double layer[1]. The net reactions are usually chemical in nature (that is, no net charge transfer). Examples include, H^+ intercalation in layered hydroxides and Li^+ insertion in metal oxides (Fig. 1a,b)[2]. Another ubiquitous example is the oxygen-incorporation reaction (OIR) occurring at the solid–gas interface (Fig. 1c). The OIR is rate determining for many energy- and environment-related technologies, including oxygen storage materials for emission control[3], solid-oxide fuel cells (SOFCs)[4], electrolysis cells[5], thermochemical water splitting cycles[6] and oxygen permeation membranes[7]. The OIR is expressed as

$$O_2 + 4e^- \rightarrow 2O^{2-} \tag{1}$$

Understanding the OIR reaction pathway is crucial for engineering and discovering catalysts, typically oxides, with high activity and stability[8,9]. Mixed ionic–electronic conductors (MIECs) have received widespread interest because they expand the effective OIR site to the gas–solid double-phase boundary, beyond the traditional triple-phase boundary between the gas, ionic and electronic conductors[10,11]. On these double-phase boundaries, oxygen ions and electrons react with oxygen adsorbates at the same active site, resulting in a reaction that involves the transfer of two oxygen ions and four electrons.

The number of charges transferred during the OIR has made it challenging to isolate the rate-determining step (RDS). Most

experimental work has focused on measuring the exchange coefficients[12] using tracer diffusion[13], conductivity and mass relaxation[14] and impedance spectroscopy[15], as well as the reaction order with respect to oxygen gas pressure (pO_2) and activation energy[16,17]. The reaction order is then used to refine microkinetic models, typically by assuming the nature of the reaction intermediates[9,18–21], and sometimes with the assistance of atomistic simulations[21,22]. While useful, these methods convolute forward and reverse reaction rate constants and do not consider crucial information about the RDS encoded in the overpotential dependence of the current density (that is, the Tafel slope). In studies in which the current density–overpotential ($j-\eta$) curves are measured, analysis of the Tafel slope is non-trivial because the slope is a natural convolution of electrostatic driving forces (surface potential) and chemical driving forces (oxygen activity in the solid state, aO_2). Similarly, analysis of the $O_2(g)$ reaction order is also non-trivial because pO_2 affects not only oxygen gas, but also the concentration of solid-state point defects at the gas–MIEC (oxide) interface[23,24], for which procedures for measurement have been developed recently[25,26]. Finally, the availability of ionic and electronic species for the OIR are generally inferred from the bulk measurements, whereas recent studies have shown that the surface chemistry and stoichiometry can differ significantly from those of the bulk. Moreover, the surface can also deviate from electroneutrality[27–29].

To isolate the RDS of the OIR, one must address the challenging task of experimentally determining the surface point defect chemistry, quantifying the electrostatic and chemical driving forces and interpreting the $O_2(g)$ reaction order and the Tafel slope simultaneously. In this work, we present an experimental and

[1]Department of Materials Science and Engineering, Stanford University, Stanford, CA, USA. [2]Department of Applied Physics, Stanford University, Stanford, CA, USA. [3]Chemical Sciences Division, Lawrence Berkeley National Laboratory, Berkeley, CA, USA. [4]Advanced Light Source, Lawrence Berkeley National Laboratory, Berkeley, CA, USA. [5]Department of Materials Science and Engineering, Massachusetts Institute of Technology, Cambridge, MA, USA. [6]Present address: The Future Laboratory, Tsinghua University, Beijing, China. [7]Present address: Center for WaSH-AID, Duke University, Durham, NC, USA. [8]Present address: Fritz Haber Institute of the Max Planck Society, Berlin, Germany. *e-mail: wchueh@stanford.edu

analysis framework and apply it to the OIR on $Pr_{0.1}Ce_{0.9}O_{2-x}$ (praseodymium cerium oxide, PCO), a promising SOFC cathode with a well-established point defect chemistry[30–32]. Combining current density–overpotential with operando surface potential and electron concentration measurements, we probe the roles of oxygen vacancies and electrons in the four-electron/two-ion MIET reaction and converge on the RDS: the dissociation of neutral molecular oxygen adsorbate. This generalizable method can also be applied to study other MIET reactions, including those occurring at solid–liquid and solid–solid interfaces.
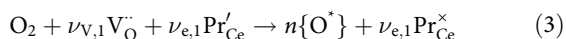
Results

Microkinetic model. Before discussing the microkinetic framework for analysing the OIR reaction order and Tafel slope, we briefly review the equilibrium point defect chemistry of PCO[30,33]. The charge carriers are small polaronic electrons and oxygen vacancies generated via the reduction of Pr^{4+} to Pr^{3+} with decreasing aO_2, as described by the following reaction written in Kröger–Vink notation:
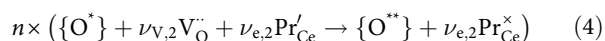
$$O_2(g) + 4Pr'_{Ce} + 2V_O^{\cdot\cdot} \leftrightarrow 4Pr_{Ce}^{\times} + 2O_O^{\times} \qquad (2)$$
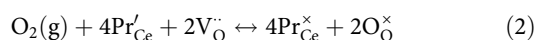
where electrons (or equivalently Pr^{3+}) are denoted by Pr'_{Ce}, oxygen vacancies by $V_O^{\cdot\cdot}$ and Pr^{4+} by $Pr_{Ce}^{\times}$. The Ce^{4+}/Ce^{3+} redox pair does not participate in the OIR under oxidizing conditions[30,33]. Bulk defect activities are shown in Supplementary Note 1.

In our microkinetic model[25], we assume that one elementary reaction step is the RDS and that all the other elementary steps occur in series and are in quasi-equilibrium. We group the elementary steps into preceding, rate-determining and following steps[1]. Rather than explicitly specifying these intermediate species, as in previous work[17,18,34,35], we use $\{O^*\}$ and $\{O^{**}\}$ to denote the reactant(s) and product(s) of the oxygen intermediate(s) involved in the RDS, respectively. The reaction pathway is then written generally as in equations (3)–(5).
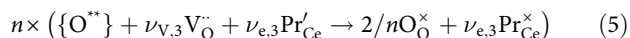
Preceding reaction:

$$O_2 + \nu_{V,1}V_O^{\cdot\cdot} + \nu_{e,1}Pr'_{Ce} \rightarrow n\{O^*\} + \nu_{e,1}Pr_{Ce}^{\times} \qquad (3)$$

RDS:

$$n \times \left(\{O^*\} + \nu_{V,2}V_O^{\cdot\cdot} + \nu_{e,2}Pr'_{Ce} \rightarrow \{O^{**}\} + \nu_{e,2}Pr_{Ce}^{\times}\right) \qquad (4)$$

Following reaction:

$$n \times \left(\{O^{**}\} + \nu_{V,3}V_O^{\cdot\cdot} + \nu_{e,3}Pr'_{Ce} \rightarrow 2/nO_O^{\times} + \nu_{e,3}Pr_{Ce}^{\times}\right) \qquad (5)$$

Here $\nu_{V,1}$, $\nu_{V,2}$ and $\nu_{V,3}$ are stoichiometric coefficients corresponding to the number of oxygen vacancies participating in the preceding, rate-determining and following steps. Analogously, $\nu_{e,1}$, $\nu_{e,2}$ and $\nu_{e,3}$ are the stoichiometric coefficients of the electrons in these steps (the possible roles of electron holes will be discussed later). Thus, these integer stoichiometric coefficients sum up to 2 and 4, respectively. The RDS can occur more than once. For example, if one O_2 molecule dissociates into two identical atomic oxygen adsorbates preceding the RDS, then the RDS will occur twice. We use n to specify the number of times that the RDS repeats per O_2 gas molecule.

Under strongly cathodic conditions, the anodic current density is negligible, and the current density (j) can be written as (detailed in Supplementary Note 3):

$$j \propto p_{O_2}^{1/n} a_{O_2}^{\lambda} \exp\left(\frac{(\beta z - \gamma_{pre}/n)e\chi}{k_B T}\right) \qquad (6)$$
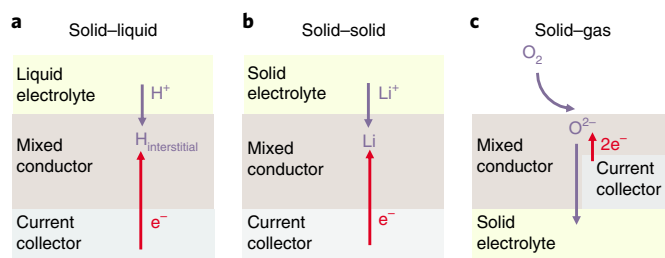

Fig. 1 | Examples of MIET reactions. a, Proton intercalation in hydroxides occurring at the liquid–solid interface. **b**, Lithium intercalation in metal oxides occurring at the solid–solid interface. **c**, Oxygen-incorporation reaction occurring at the solid–gas interface.

where

$$\lambda = \left(\frac{\nu_{V,1}}{n} + \nu_{V,2}\right)\frac{\partial \log a\left(V_O^{\cdot\cdot}\right)}{\partial \log a_{O_2}}\bigg|_{T,p_{O_2}} + \left(\frac{\nu_{e,1}}{n} + \nu_{e,2}\right)\frac{\partial \log a\left(Pr'_{Ce}\right)}{\partial \log a_{O_2}}\bigg|_{T,p_{O_2}} - \frac{\nu_{e,1}}{n}\frac{\partial \log a\left(Pr_{Ce}^{\times}\right)}{\partial \log a_{O_2}}\bigg|_{T,p_{O_2}} \qquad (7)$$

$$a_{O_2} = p_{O_2}\exp\left(\frac{4e\eta}{k_B T}\right) \qquad (8)$$

Equation (8), which is the Nernst equation (k_B is the Boltzmann constant and T the temperature), describes the relationship between the oxygen partial pressure in the gas phase and the oxygen activity in the electrode. There are two degrees of freedom between overpotential (η), p_{O_2} and a_{O_2}. For clarity, constants and equilibrium concentrations and potential are not shown in equation (6). Here, z is the total number of electrons and/or ions migrating across the gas–solid interface in the RDS, β is the symmetry parameter of this electrochemical step (if $z \neq 0$) and γ_{pre} determines the dependence of the preceding equilibrium on the surface potential χ.

The kinetic parameters n and λ in equation (6) reflect the reaction mechanism. The term n, as mentioned, represents the number of times that the RDS repeats and directly describes the dependence of the current density on p_{O_2}, and λ is a measure of the overall dependence of point defect activities on a_{O_2}. It should be noted that, for a given combination of a_{O_2}, p_{O_2} and overpotential, the electrode and the surface chemistry can be unique. Therefore, n can depend on a_{O_2}, and likewise λ can depend on p_{O_2}. The model reconciles adsorbate chemistry with point defect chemistry at the solid–gas interface under electrochemical bias. Next, we obtain n and λ experimentally, and shed light on the kinetics of MIET steps in the OIR.

Electrochemical characteristics. We fabricated 150-nm-thick, dense, thin-film PCO electrodes on single-crystalline yttria-stabilized zirconia (YSZ) solid electrolytes via pulsed-laser deposition (see Methods). A buried Pt microfabricated current collector is used to eliminate its contribution to the reaction pathway and to ensure uniform electronic current collection. An oversized and highly active counter electrode was also used to eliminate contributions from the counter electrode. In this cell configuration, electrochemical polarization at the Pt–YSZ interface drives the chemical OIR at the gas–solid interface. We note that electronic conductivity in PCO decreases with p_{O_2}: above $\sim 10^{-3}$ atm, impedance spectroscopy indicates an in-plane electronic transport gradient. This is a result of the geometry of the microfabricated current collector employed. For this reason, we limit the p_{O_2} to below $\sim 10^{-3}$ atm, which is lower than that in typical SOFC cathodes.
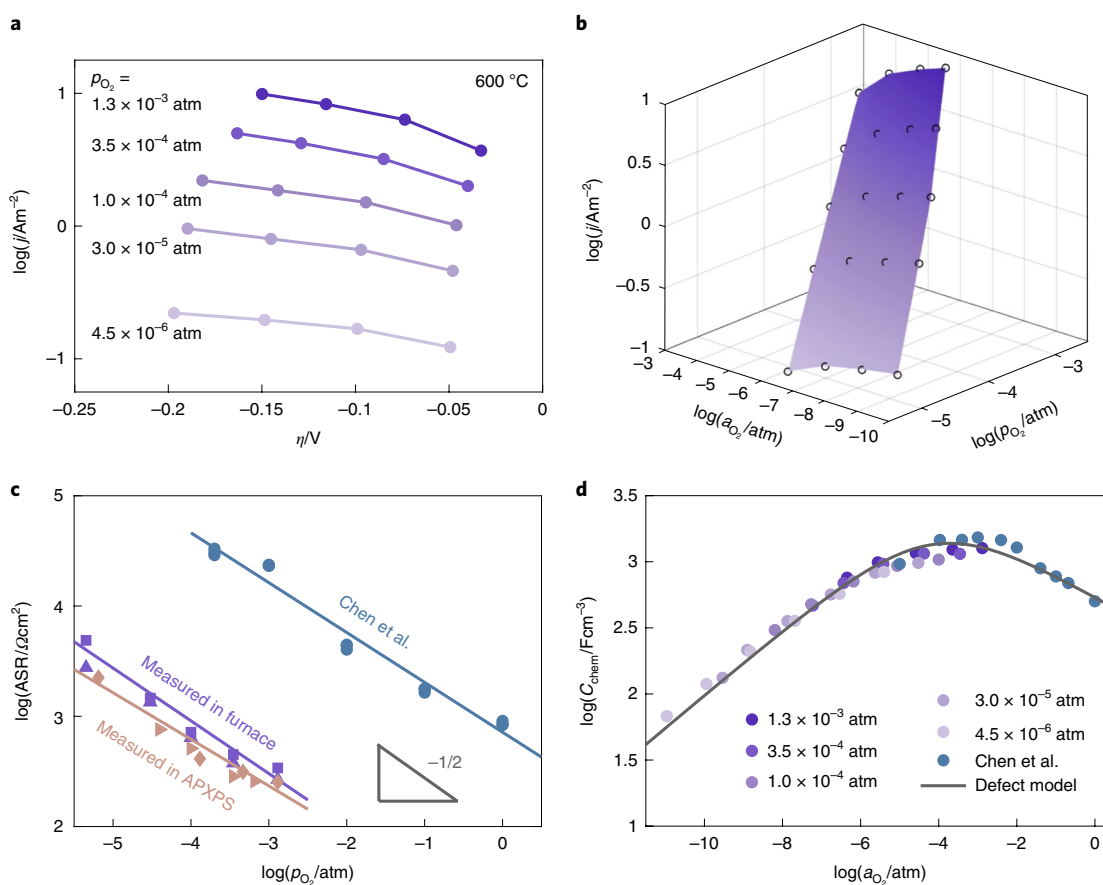
Fig. 2 | Electrochemical measurement results. a, Overpotential dependence of current density of PCO at 600 °C. The symbols indicate experimental data. The lines are used to guide the eye. The overpotential is ohmic-corrected and validated by C_{chem} and peak shift in APXPS spectra. **b**, Reconstruction of **a** versus pO_2 and aO_2 using equation (8). The curved surface is a two-dimensional fitting of the experimental results. **c**, pO_2 dependence of open circuit area-specific resistance (ASR) of PCO at 600 °C. The purple symbols indicate experimental data from this study, measured in a tube furnace. The peach symbols indicate experimental data from this study, measured in the APXPS chamber. The navy symbols indicate experimental data from the literature, measured in a tube furnace, using a quartz tube as the testing tube and Au paste as the current collector[36]. Solid lines represent linear fitting of the experimental data. **d**, aO_2 dependence of volume-specific chemical capacitance (C_{chem}) of the PCO film at 600 °C. The symbols indicate experimental data in this study compared with the literature[36]. The solid line represents fit of the bulk defect model to experimental data.

Current density–overpotential curves were measured as functions of pO_2 at 600 °C, using both a conventional electrochemical rig and a button heater inside an ambient pressure X-ray photoelectron spectroscopy (APXPS) chamber. The overpotential-dependent current density at different pO_2 values at 600 °C is shown in Fig. 2a. We then calculated aO_2 via the Nernst equation (equation (8)), and plotted the current density as a function of both aO_2 and pO_2 (Fig. 2b)[26]. We verified that the electrode had reached steady state and that degradation was not convoluting the measurement (Supplementary Fig. 1a). Reproducibility was excellent amongst four cells (Fig. 2c). We note that the area-specific resistance at open circuit is approximately two orders of magnitude lower than that reported in a previous study[36], although the reaction order with pO_2 is comparable. We attribute this improvement to the lower impurity level in this study: only Au and Pt wires and alumina were in contact with the sample and the hot gas, in contrast to previous measurements[37]. The reaction order measured in this study also agrees broadly with Simons et al., in which a reaction order of 0.67 was measured by a mass relaxation method on PCO[38]. We also carried out impedance spectroscopy under bias (Supplementary Fig. 1b). The Nyquist plot is well described by a simple serial resistor–capacitor network. For ohmic-corrected overpotentials from −200 to 0 mV, the absence of a Warburg-like feature confirms that electronic

and ionic diffusion gradients are small, even under bias, indicating that our cell is limited by the OIR surface reaction. Nevertheless, we cannot completely rule out equilibrium or transport gradients in the near-surface region. If such a gradient exists, one has to relate the oxygen activity at the surface to that in the bulk.

The application of equation (8) requires precise measurement and control of overpotential, which is challenging for solid-state electrochemical cells[39,40]. To confirm that we have indeed measured the overpotential accurately, we used the chemical capacitance (C_{chem}) of PCO as an internal gauge of aO_2 (Fig. 2d). We find that C_{chem} is only a function of aO_2 at open circuit and under bias, that is, values measured at different aO_2 (either by changing pO_2 or changing the overpotential) collapse onto a single line. This directly confirms that the overpotential was determined accurately. Fitting a bulk defect chemical model to C_{chem} in our thin-film electrode gives defect formation energetics comparable to bulk values (Supplementary Note 2).

Operando characterization of gas–solid interface. As localized electrons on the PCO surface are reactants of the OIR, we used operando Pr M-edge X-ray absorption spectroscopy (XAS) in partial electron-yield detection mode to determine the near-surface oxidation state of PCO as a function of overpotential (Fig. 3a,b).
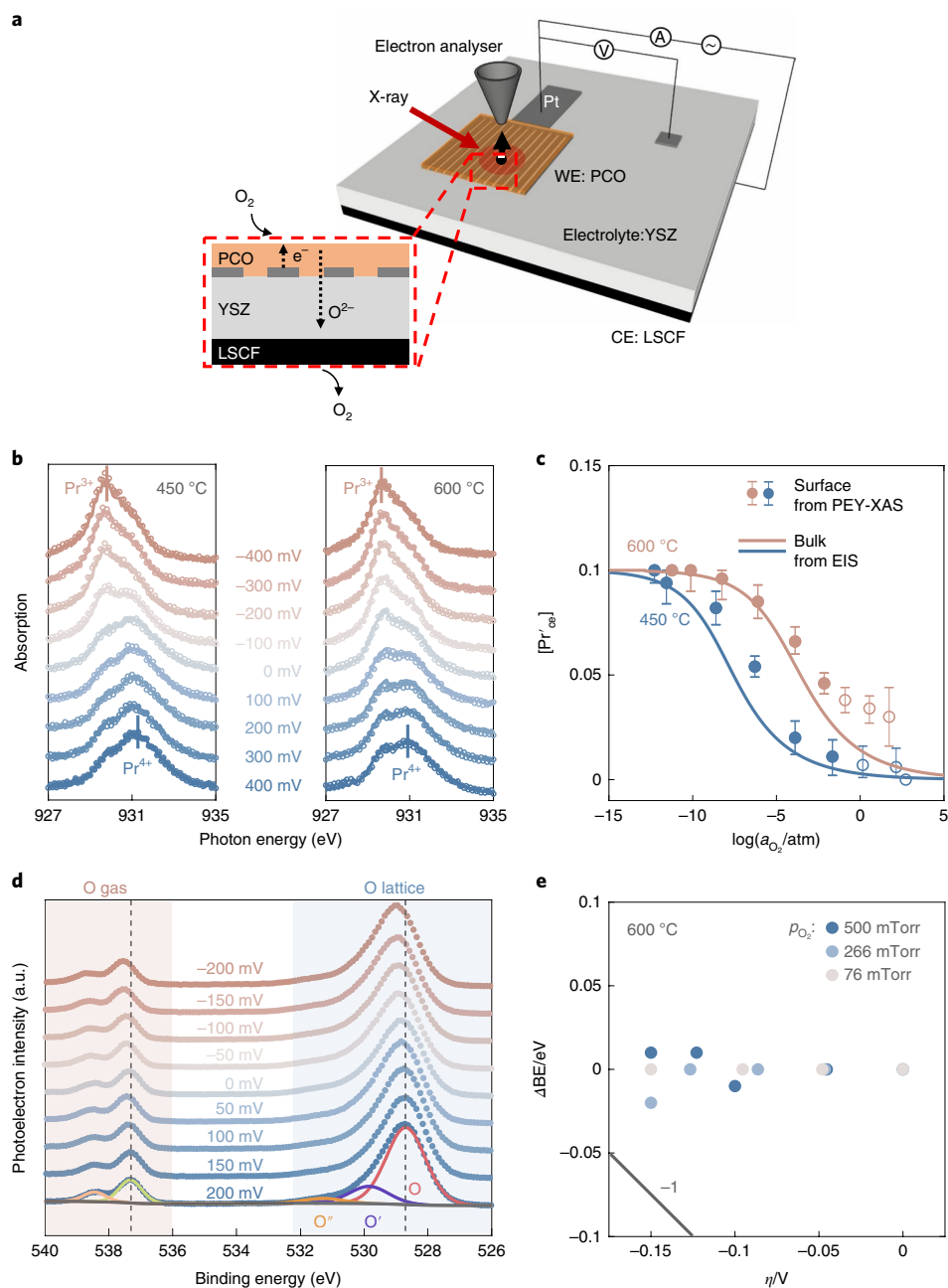
Fig. 3 | Experimental set-up and evolution of surface electron concentration and surface potential with overpotential. a, A schematic depicting the experimental set-up. The cell is based on a YSZ solid-oxide electrolyte, with dense PCO as the working electrode (WE) and $(La_{0.6}Sr_{0.4})(Co_{0.2}Fe_{0.8})O_3$ (LSCF) as the counter electrode (CE). Patterned Pt is embedded in the PCO thin film for efficient current collection. **b**, Pr M_4-edge measured by ambient pressure X-ray absorption spectroscopy (XAS) in partial electron-yield (PEY) detection mode at 450 °C and 600 °C at $pO_2 = 100$ mTorr, as a function of overpotential. The symbols are experimental data. The lines are linear combination fitting of spectra under the most oxidized (450 °C, +400 mV) and most reduced (600 °C, −400 mV) conditions. **c**, aO_2 dependence of the small polaron concentration (Pr^{3+} in PCO) on the surface measured by APXAS (symbols), and in the bulk calculated using chemical capacitance data (solid lines). The aO_2 of the filled symbols were validated by chemical capacitance. The aO_2 of the empty symbols could not be validated by chemical capacitance because their electrochemical impedance spectra (EIS) are highly distorted. Error bars are reported for an approximate 99% confidence of the linear combination. **d**, Normalized O 1s APXPS spectra at various overpotential at 600 °C in 6.6×10^{-4} atm (500 mTorr). The overpotential is validated by C_{chem}. For lattice oxygen peaks, the main peak in red and shoulder peaks in purple and orange are due to lattice oxygen (O), oxygen bonded to the Si impurity (O′) and surface O (O′′), respectively. Spectra were taken at a photon energy of 690 eV corresponding to a probing depth of 0.6 nm. The BE is calibrated with the Au $4f_{7/2}$ peak of gold foil connected to the PCO electrode. a.u., arbitrary units. **e**, The shift of surface potential with overpotential at 600 °C. The values are plotted relative to open-circuit conditions.

Two end members (spectra measured at +400 mV and 450 °C and spectra measured at −400 mV and 600 °C) are consistent with the Pr^{4+} and Pr^{3+} states, respectively[41,42] (Supplementary Fig. 6). We then

obtained the fraction of Pr in the 3+ state, [Pr^{3+}], through a linear combination fitting consisting of the end members (Fig. 3b,c and Supplementary Fig. 7). The results are comparable to those
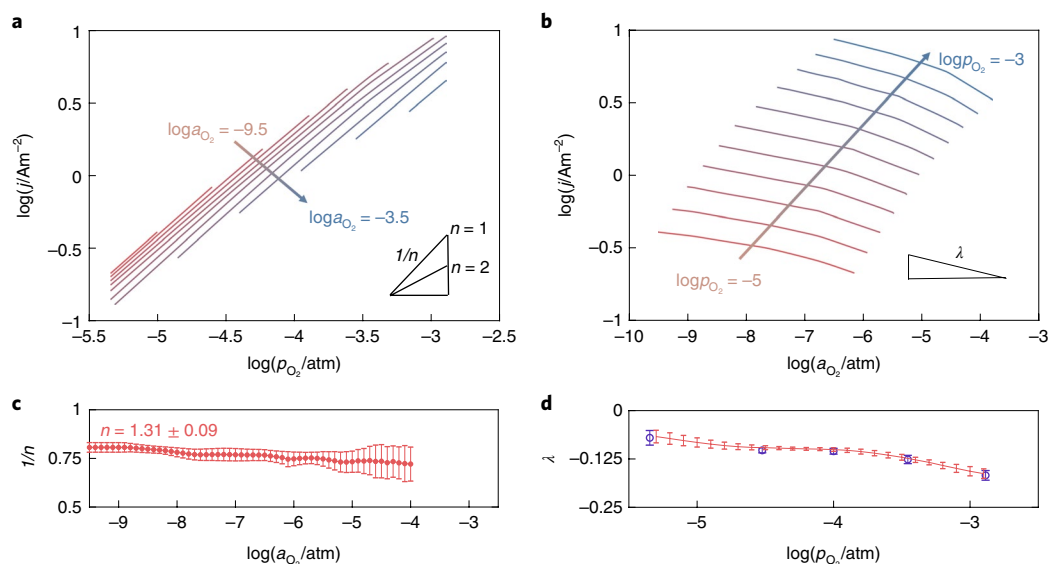
Fig. 4 | Reaction orders for OIR. a, pO_2 dependence of current density at several constant aO_2. **b**, aO_2 dependence of current density at several constant pO_2. **c,d**, The reaction orders $1/n$ and λ, calculated from **a** and **b**, respectively. The error bars are calculated from three electrodes. The blue symbols in **d** indicate specific pO_2s shown in Fig. 2a.

reported by Lu et al. at 450 °C (ref. [43]). Figure 3c compares the surface defect concentrations to bulk values. Praseodymium becomes fully reduced to 3+ at comparable aO_2, both at the surface and in the bulk; at more oxidizing aO_2, the surface is slightly more reduced than the bulk. Direct quantification of surface oxygen vacancies, the other important participant in the OIR, was not possible, probably reflecting a low concentration due to PCO having a bulk oxygen vacancy concentration of $\leq 2.5\%$ (Supplementary Fig. 4c).

The presence of charged adsorbates and charged ions near the surface establishes a potential drop, χ, with deviation relative to the open-circuit value contributing to the reaction rate[23,25,44]. For a metal electrode, such a potential drop is trivially related to the overpotential. However, for an MIEC, it cannot be inferred from electrochemical measurement, nor independently controlled. Here, we estimate χ using operando APXPS via shifts of O 1s photoemission peaks[45–47]. Measurements were performed at oxygen gas pressures ranging from 0.03 to 1 Torr O_2 atmosphere at 600 °C. Specifically, we compare the binding energy (BE) of oxygen gas and lattice oxygen on the PCO surface (Fig. 3d), which was carried out at the same time as the XAS measurement. For the lattice oxygen peak, we identified a total of three oxygen species at an information depth of ~0.6 nm (for the definition of surface sensitivity, see ref. [45]). On the basis of earlier photoemission studies, we assigned the most intense peak (the blue peak denoted as O) to bulk-like lattice oxygen in PCO[45]. The two smaller peaks at relative BEs of ~1.2 and ~2.6 eV (the purple peak denoted as O′ and cyan peak denoted as O″, respectively) are attributed to oxygen bonded to segregated silicon impurities and surface adsorbates. These relative BEs between O′, O″ and lattice O did not change with bias or pO_2 (Supplementary Fig. 4b).

We now consider the BEs of the oxygen gas and lattice oxygen, the difference in which is related to the surface potential[45]. As shown in Fig. 3d, the spectra of the oxygen gas and oxygen core levels both shift systematically with applied overpotential. Quantitative analysis reveals that both the oxygen gas and oxygen lattice core levels shifted by approximately 1 eV per 1 V of applied overpotential (Supplementary Fig. 4a). This means that the surface potential is essentially constant under all conditions examined (Fig. 3e), simplifying the current density expression in equation (6) to $j \propto p_{O_2}^{1/n} a_{O_2}^{\lambda}$. This result is consistent with the findings of our

recent study of CeO_{2-x}, in which only strongly polar adsorbates (such as OH^-) induce a change in χ with overpotential[45].

Analysis of current density–overpotential curves. To obtain the $O_2(g)$ reaction order ($1/n$), the slope of $\log j - \log pO_2$ was evaluated at constant aO_2 values (Fig. 4a); n has an average of ~1.3 from measurement of three electrodes and is largely independent of aO_2, indicating that the RDS occurs once (Fig. 4c). This directly suggests that the RDS involves a molecular oxygen intermediate. The deviation from 1 may be explained by non-dilute adsorption surface sites (details in Supplementary Note 9) and/or the emergence of co-limiting RDSs[48]. We followed a similar procedure to obtain λ, the reaction order on aO_2 (Fig. 4b,d). We obtain an average value for λ of -0.13, which tends to 0 at low aO_2.

At first glance, if λ is given, it appears to be straightforward to use equation (7) to solve the combination of stoichiometric coefficients ($\nu_{V,i}$ and $\nu_{e,i}$) in equations (3)–(5) to identify the MIET pathway. These coefficients enable the number of electrons and oxygen vacancies before, during and after the RDS to be determined. However, we are missing one crucial parameter. As shown in equation (7), interpreting λ requires knowing the oxygen vacancy concentration at the PCO surface, which could not be determined experimentally due to its dilute concentration. While it is common to invoke the electroneutrality approximation to estimate this quantity, the surface may not be electroneutral[27–29].

Here, we developed a procedure to estimate these stoichiometric coefficients without knowing the oxygen vacancy concentration. In total, we consider 108 combinations of integer values of n, $\nu_{V,i}$ and $\nu_{e,i}$ (Supplementary Table 2). Each combination corresponds to a possible MIET pathway. Knowing that the OIR proceeds via a molecular pathway, we excluded all the combinations containing $n = 2$, leaving 90 possible pathways. Next, we simulate how λ varies with pO_2 for these pathways and compare them to the experimentally measured values. For $\frac{\partial \log[Pr'_{Ce}]}{\partial \log a_{O_2}}$, we used the surface values measured by operando XAS (since $[Pr'_{Ce}] \ll 1$). To address the issue of not knowing the surface oxygen vacancy concentration, we specifically investigate three limiting scenarios. First, we consider $2[V_O^{\cdot\cdot}] = [Pr^{3+}]$, which corresponds to an electroneutral surface. Second, we consider $\frac{\partial \log[V_O^{\cdot\cdot}]}{\partial \log a_{O_2}} = 0$, whereby oxygen vacancies are
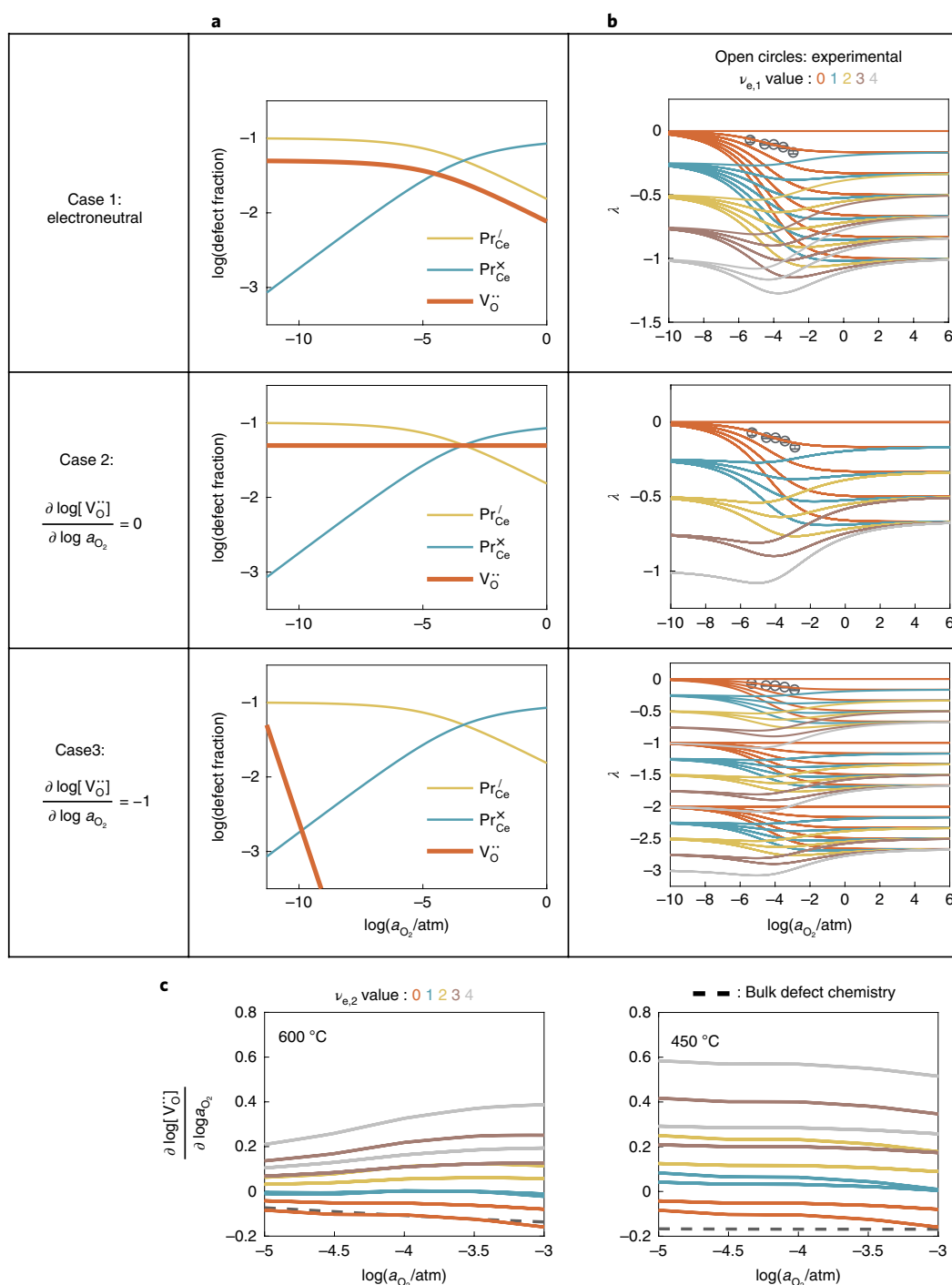
Fig. 5 | Obtaining reaction stoichiometric coefficients ($\nu_{V,i}$ and $\nu_{e,i}$) by analysing λ. a, The dependence of simulated defect concentrations on aO_2 in PCO at 600 °C, with different $\frac{\partial \log[V_O^{..}]}{\partial \log a_{O_2}}$ as noted. **b**, The simulated aO_2 dependence of λ. The solid lines are calculated by equation (8), with the defect concentrations as shown in **a**. Different lines are calculated with different $\nu_{e,1}$ values, as indicated by different colours. The symbols are experimental data. **c**, The aO_2 dependence of $\frac{\partial \log[V_O^{..}]}{\partial \log a_{O_2}}$ at 600 °C and 450 °C. The solid lines are back-calculated from the experimental λ using equation (8). Different lines are calculated with different $\nu_{e,2}$ values, as indicated by different colours. The dashed line shows bulk experimental values.

decoupled from electrons leading to build-up of charge, and the surface is saturated with oxygen vacancies such that they do not change with oxygen partial pressure. Finally, we consider $\frac{\partial \log[V_O^{..}]}{\partial \log a_{O_2}} = -1$, which represents a scenario in which oxygen vacancy concentration decreases with oxygen partial pressure more sharply than in the

electroneutral case: defect–defect interactions and other non-idealities could lead to this situation. The simulated defect concentrations under those scenarios are plotted in Fig. 5a, and the corresponding λ values for the 90 candidate molecular pathways are shown in Fig. 5b. Experimentally, we observed that λ tends to 0 under reducing conditions (low aO_2). For all three oxygen vacancy limits

	$\nu_{V,1}$	$\nu_{V,2}$	$\nu_{V,3}$	$\nu_{e,1}$	$\nu_{e,2}$	$\nu_{e,3}$	Initial state of RDS	Final state of RDS
A	0	0	2	0	0	4		
B	0	1	1	0	0	4		
C	0	2	0	0	0	4		
D	1	0	1	0	0	4		
E	1	1	0	0	0	4		
F	2	0	0	0	0	4		

Fig. 6 | Reaction mechanism. Combinations of stoichiometric coefficients that satisfy the condition $\nu_{e,1} = \nu_{e,2} = 0$ with their corresponding RDS and final state. The shaded combinations are unlikely. Here $\nu_{V,1}$, $\nu_{V,2}$ and $\nu_{V,3}$ are stoichiometric coefficients corresponding to the number of oxygen vacancies participating in the preceding, rate-determining and following steps. Analogously, $\nu_{e,1}$, $\nu_{e,2}$ and $\nu_{e,3}$ are the stoichiometric coefficients of the electrons in these steps.

considered, only $\nu_{e,1} = 0$ (no electrons transferred before RDS) yields this behaviour (Fig. 5b). Indeed, satisfactory fits to λ can be obtained only for $\nu_{e,1} = 0$, while other values of $\nu_{e,1}$ (1 to 4) yield λ values that are inconsistent with the experimentally measured values. This is because the third term in equation (7) scales directly with $\nu_{e,1}$. With this insight, the number of possible pathways then decreases considerably from 90 to 30.

To further converge on the reaction pathway, we take the experimental value of λ, and back-calculate $\frac{\partial \log[V_O^{\cdot\cdot}]}{\partial \log a_{O_2}}$ for the 30 remaining combinations of stoichiometric numbers of electrons and oxygen vacancies (Fig. 5c). We exclude all the combinations that give a positive $\frac{\partial \log[V_O^{\cdot\cdot}]}{\partial \log a_{O_2}}$ value because the surface oxygen vacancy concentration is unlikely to increase with a_{O_2}. This constraint further lowers the possible combinations from 30 to 6; these six combinations are tabulated in Fig. 6 along with their corresponding RDS. Notably, $\nu_{e,1}$ (number of electrons transferred before the RDS) and $\nu_{e,2}$ (number of electrons transferred during the RDS) are zero for all the combinations in Fig. 6. In other words, electrons are not involved before or during the RDS. In fact, these six reaction pathways are the only ones with this feature amongst the original 108 combinations.

Now, we take a closer look at these remaining six possibilities. Reaction pathway A can be easily excluded, as it results in a zero O_2 reaction order ($\lambda = 0$) for all pO_2, which is inconsistent with the experiments in Fig. 4d. This result is natural as the RDS in reaction A corresponds to $O_2(g)$ adsorption, which leads to a current density that is independent of the defect concentration in the bulk (hence, $\lambda = 0$). Reaction pathway F is also unlikely, as it means that the $O_2(g)$ molecule has been incorporated into a cluster containing two adjacent oxygen vacancies before the RDS (because two oxygen vacancies were transferred before the RDS while the oxygen intermediate remained molecular). The remaining four reaction pathways, B–E,

share two common features: (1) the RDS involves a molecular oxygen adsorbate and (2) electrons are not transferred before or during the RDS. In other words, the RDS is an O_2 dissociation process that involves neutral O_2 (without having been reduced). The differences between the four pathways concern whether 0, 1 or 2 oxygen vacancies are involved in the RDS. For pathways B and C, the initial state involves molecular oxygen adsorbates, whereas for pathways D and E, the initial state involves molecular oxygen already incorporated into an oxygen vacancy. We can also differentiate the pathways on the basis of the final state. In pathways B and D, the final state is one incorporated oxygen ion and one atomic oxygen adsorbate; in pathway C and E, the final state is two incorporated oxygen ions. Our conclusion is consistent with a recent study by Schaube et al. These authors investigated the RDS of PCO using a pulsed isotope exchange method, and found that molecular oxygen species are involved in the RDS (in addition to oxygen vacancies)[49].

We note that in MIECs, such as $SrTi_{1-x}Fe_xO_{3-\delta}$, it has been proposed that minority, rather than majority, electronic species participate in the RDS[34]. For completeness, we simulated λ assuming that holes (presumably oxygen holes) are involved in the RDS. The reaction order is not sensitive to whether no electrons or some holes are involved (Supplementary Note 10). Our analysis indicates that studies under anodic overpotentials are needed, which are being pursued. Nevertheless, this ambiguity does not affect the conclusion that the RDS is probably the dissociation of a neutral O_2 adsorbate.

This insight into the reaction mechanism can be used to improve the catalytic activity of ceria as well as other materials for the OIR. Because electrons are not involved before or during the RDS, lowering the electron transfer barrier or increasing concentrations are not expected to substantially improve the surface catalytic activity. Instead, efforts should be focused on decreasing the barrier height for O_2 dissociation and for oxygen incorporation into vacancies,

and increasing concentrations[50]. This insight may also apply to other oxygen-incorporation catalysts that are limited by the availability of surface oxygen vacancies.

In summary, we developed a generalizable experimental and analysis framework to identify the RDS for the oxygen-incorporation reaction on $Pr_{0.1}Ce_{0.9}O_{2-x}$, a promising cathode for solid-oxide fuel cells. By simultaneously measuring how current density depends on oxygen partial pressure and overpotential, as well as how the surface electron concentration and electrostatic potential vary, we eliminate the vast majority of the candidate MIET reaction pathways. The rich information encoded in the oxygen partial pressure and overpotential dependences makes it possible to converge on four possible reaction pathways, even though surface oxygen vacancy concentration could not be measured directly. The robust conclusion that the RDS is probably the dissociation of neutral molecular oxygen adsorbate provides an important mechanistic insight that could further guide the optimization of oxygen-incorporation (electro)catalysts. This analysis method can be straightforwardly extended to other oxygen-ion-conducting electrodes, as well as to other chemistries, to unravel the microkinetics of MIET reactions.

Methods

Sample preparation. Thin-film electrochemical cells were fabricated on $10 \times 10 \times 0.5$ mm³ (100) $Y_{0.16}Zr_{0.84}O_{1.92}$ (YSZ) single-crystal substrates (MTI Corporation), which served as the oxygen-ion-conducting solid electrolyte. The fabrication procedure, described in chronological order, is as follows. First, a Pt-patterned current collector (5 μm line width and 30 μm) was fabricated on the smooth side of the substrate using metal lift-off photolithography. The fabrication procedure was as reported previously[51]. Then, 200-nm-thick LSCF ($La_{0.6}Sr_{0.4}Co_{0.2}Fe_{0.8}O_{3-δ}$) thin films were deposited on the back of the YSZ as the counter electrode using pulsed-laser deposition (PLD). A 20-nm-thick $Sm_{0.2}Ce_{0.8}O_{1.9}$ buffer layer was also deposited to suppress cation interdiffusion between the YSZ and LSCF thin film. The PLD deposition was performed at 700 °C and 5 mTorr O_2 with a laser fluence of 1.5 J cm^{-2} at 10 Hz and a substrate-to-target distance of 70 mm. The high activity and large area of the counter electrode guaranteed that the counter-electrode reaction did not limit the cell performance. Finally, 150-nm-thick $Pr_{0.1}Ce_{0.9}O_2$ (PCO) thin films were deposited using PLD. An Inconel shadow mask, with an opening of 0.5×2 mm², was employed to deposit PCO on top of the Pt-patterned current collector. The PLD deposition was performed at 700 °C and 5 mTorr O_2 with a laser fluence of 1.5 J cm^{-2} at 10 Hz and a substrate-to-target distance of 70 mm.

A solid-state method was used to prepare PCO polycrystalline targets. Pr_6O_{11} and CeO_2 high-purity powders (99.99%, Sigma-Aldrich) were weighed according to the desired stoichiometry, ground in a mortar and then pressed into 1-inch-radius pellets. The as-obtained pellets were calcined at 900 °C for 5 h and then at 1,250 °C for 9 h in Ar to obtain dense targets for PLD. A similar procedure was used to fabricate the LSCF target, the details for which were previously reported[52].

Sample characterization. X-ray diffraction patterns of the as-deposited thin films were obtained in the 2θ range of 20–80° (Panalytical X'Pert PRO, CuKα radiation). The films crystallized in the cubic fluorite structure (Supplementary Fig. 3). The film thickness was determined using a surface profilometer (Dektak 150, Veeco). The thin-film composition was examined using inductively coupled plasma–mass spectrometry (ICP–MS, Thermo Scientific XSERIES 2). The surface morphology was characterized using atomic force microscopy (Park Systems XE-100).

Electrochemical measurements. Electrochemical measurements were performed using a custom electrochemical testing system that did not use any metal paste or silicon-containing materials. The aim was to use high-purity alumina and noble metals to reduce or eliminate the convoluting effects of binding agents in metal pastes, as these agents can combust or volatilize. A gas manifold of synthetic high-purity gas mixtures of O_2 balanced with Ar was used to control the oxygen partial pressure, pO_2, using MKS P4B mass-flow controllers.

Electrochemical APXPS. The measurement was carried out at beamlines 11.0.2 and 9.3.2 of the Advanced Light Source at Lawrence Berkeley National Laboratory[53]. The samples were mounted onto a gold mesh (counter) on the ceramic heater of a custom-made heating and biasing stage[54]. Pt–Ir (10%–20% Ir) wires were used as an electrical contact and to hold the working electrode onto the heater. The temperature was determined from the ohmic offset of YSZ using electrochemical impedance spectroscopy (Biologic SP-300 potentiostat) of model dense Pt film devices calibrated in a tube furnace with a thermocouple near the device. The entire APXPS experiment was performed under defined bias, and the alternating voltage perturbation was 10 mV.

Electrochemical ambient pressure XAS. Operando XAS in partial electron-yield detection mode was measured at 100 mTorr O_2 at 450 and 600 °C at beamline 11.0.2 of the Advanced Light Source at Lawrence Berkeley National Laboratory[53]. The sample mounting, temperature calibration and electrochemical measurements were the same as those used for the APXPS experiment. The background was removed from the spectra by fitting a line to the Pr M_4 pre-edge. The spectra were subsequently normalized by the Pr M_5 post-edge.

Data availability
Source data that support the findings of this study are available from the corresponding author on request.

References
1. Bard, A. J. & Faulkner, L. R. *Electrochemical Methods: Fundamentals and Applications* 2nd edn (Wiley, 2000).
2. Li, Y. & Chueh, W. C. Electrochemical and chemical insertion for energy transformation and switching. *Annu. Rev. Mater. Res.* **48**, 1–29 (2018).
3. Yao, H. C. & Yao, Y. F. Y. Ceria in automotive exhaust catalysts. I. Oxygen storage. *J. Catal.* **86**, 254–265 (1984).
4. Graves, C., Ebbesen, S. D., Jensen, S. H., Simonsen, S. B. & Mogensen, M. B. Eliminating degradation in solid oxide electrochemical cells by reversible operation. *Nat. Mater.* **14**, 239–244 (2015).
5. Irvine, J. T. S. et al. Evolution of the electrochemical interface in high-temperature fuel cells and electrolysers. *Nat. Energy* **1**, 15014 (2016).
6. Chueh, W. C. et al. High-flux solar-driven thermochemical dissociation of CO₂ and H₂O using nonstoichiometric ceria. *Science* **330**, 1797–1801 (2010).
7. Shao, Z. et al. Investigation of the permeation behavior and stability of a $Ba_{0.5}Sr_{0.5}Co_{0.8}Fe_{0.2}O_{3-δ}$ oxygen membrane. *J. Memb. Sci.* **172**, 177–188 (2000).
8. Riva, M. et al. Influence of surface atomic structure demonstrated on oxygen incorporation mechanism at a model perovskite oxide. *Nat. Commun.* **9**, 3710 (2018).
9. Merkle, R. & Maier, J. How is oxygen incorporated into oxides? A comprehensive kinetic study of a simple solid-state reaction with $SrTiO_3$ as a model material. *Angew. Chem. Int. Ed. Engl.* **47**, 3874–3894 (2008).
10. Adler, S. B. Factors governing oxygen reduction in solid oxide fuel cell cathodes. *Chem. Rev.* **104**, 4791–4843 (2004).
11. Chueh, W. C., Hao, Y., Jung, W. & Haile, S. M. High electrochemical activity of the oxide phase in model ceria-Pt and ceria-Ni composite anodes. *Nat. Mater.* **11**, 155–161 (2012).
12. Maier, J. On the correlation of macroscopic and microscopic rate constants in solid state chemistry. *Solid State Ion.* **112**, 197–228 (1998).
13. Kilner, J. A., De Souza, R. A. & Fullarton, I. C. Surface exchange of oxygen in mixed conducting perovskite oxides. *Solid State Ion.* **86–88**, 703–709 (1996).
14. Gopal, C. B. & Haile, S. M. An electrical conductivity relaxation study of oxygen transport in samarium doped ceria. *J. Mater. Chem. A* **2**, 2405–2417 (2014).
15. Baumann, F. S. et al. Quantitative comparison of mixed conducting SOFC cathode materials by means of thin film model electrodes. *J. Electrochem. Soc.* **154**, B931–B941 (2007).
16. Fleig, J., Merkle, R. & Maier, J. The $p(O_2)$ dependence of oxygen surface coverage and exchange current density of mixed conducting oxide electrodes: model considerations. *Phys. Chem. Chem. Phys.* **9**, 2713–2723 (2007).
17. Merkle, R. & Maier, J. Oxygen incorporation into Fe-doped $SrTiO_3$: mechanistic interpretation of the surface reaction. *Phys. Chem. Chem. Phys.* **4**, 4140–4148 (2002).
18. De Souza, R. A. A universal empirical expression for the isotope surface exchange coefficients (k*) of acceptor-doped perovskite and fluorite oxides. *Phys. Chem. Chem. Phys.* **8**, 890–897 (2006).
19. Jung, W. & Tuller, H. L. Investigation of surface Sr segregation in model thin film solid oxide fuel cell perovskite electrodes. *Energy Environ. Sci.* **5**, 5370–5378 (2012).
20. Adler, S. B., Chen, X. Y. & Wilson, J. R. Mechanisms and rate laws for oxygen exchange on mixed-conducting oxide surfaces. *J. Catal.* **245**, 91–109 (2007).
21. Cao, Y., Gadre, M. J., Ngo, A. T., Adler, S. B. & Morgan, D. D. Factors controlling surface oxygen exchange in oxides. *Nat. Commun.* **10**, 1346 (2019).
22. Mastrikov, Y. A., Merkle, R., Heifets, E., Kotomin, E. A. & Maier, J. Pathways for oxygen incorporation in mixed conducting perovskites: a DFT-based mechanistic analysis for (La, Sr)MnO₃₋δ. *J. Phys. Chem. C* **114**, 3017–3027 (2010).
23. Fleig, J. J. On the current–voltage characteristics of charge transfer reactions at mixed conducting electrodes on solid electrolytes. *Phys. Chem. Chem. Phys.* **7**, 2027–2037 (2005).
24. Tuller, H. L. & Bishop, S. R. Point defects in oxides: tailoring materials through defect engineering. *Annu. Rev. Mater. Res.* **41**, 369–398 (2011).

25. Guan, Z., Chen, D. & Chueh, W. C. Analyzing the dependence of oxygen incorporation current density on overpotential and oxygen partial pressure in mixed conducting oxide electrodes. *Phys. Chem. Chem. Phys.* **19**, 23414–23424 (2017).

26. Schmid, A., Rupp, G. M. & Fleig, J. Voltage and partial pressure dependent defect chemistry in (La,Sr)FeO$_{3-\delta}$ thin films investigated by chemical capacitance measurements. *Phys. Chem. Chem. Phys.* **20**, 12016–12026 (2018).

27. Zurhelle, A. F., Tong, X., Klein, A., Mebane, D. S. & De Souza, R. A. A space-charge treatment of the increased concentration of reactive species at the surface of a ceria solid solution. *Angew. Chem. Int. Ed. Engl.* **56**, 14516–14520 (2017).

28. De Souza, R. A. The formation of equilibrium space-charge zones at grain boundaries in the perovskite oxide SrTiO$_3$. *Phys. Chem. Chem. Phys.* **11**, 9939–9969 (2009).

29. De Souza, R. A. & Martin, M. Using $^{18}O/^{16}O$ exchange to probe an equilibrium space-charge layer at the surface of a crystalline oxide: method and application. *Phys. Chem. Chem. Phys.* **10**, 2356–2367 (2008).

30. Chen, D., Bishop, S. R. & Tuller, H. L. Non-stoichiometry in oxide thin films: a chemical capacitance study of the praseodymium-cerium oxide system. *Adv. Funct. Mater.* **23**, 2168–2174 (2013).

31. Chen, D., Bishop, S. R. & Tuller, H. L. Praseodymium-cerium oxide thin film cathodes: study of oxygen reduction reaction kinetics. *J. Electroceram.* **28**, 62–69 (2012).

32. Seo, H. G., Choi, Y. & Jung, W. Exceptionally enhanced electrode activity of (Pr,Ce)O$_{2-\delta}$-based cathodes for thin-film solid oxide fuel cells. *Adv. Energy Mater.* **1703647**, 1–7 (2018).

33. Bishop, S. R., Stefanik, T. S. & Tuller, H. L. Electrical conductivity and defect equilibria of Pr$_{0.1}$Ce$_{0.9}$O$_{2-\delta}$. *Phys. Chem. Chem. Phys.* **13**, 10165–10173 (2011).

34. Jung, W. & Tuller, H. L. A new model describing solid oxide fuel cell cathode kinetics: model thin film SrTi$_{1-x}$Fe$_x$O$_{3-\delta}$ mixed conducting oxides-a case study. *Adv. Energy Mater* **1**, 1184 (2011).

35. Kuklja, M. M., Kotomin, Ea, Merkle, R., Mastrikov, Ya & Maier, J. Combined theoretical and experimental analysis of processes determining cathode performance in solid oxide fuel cells. *Phys. Chem. Chem. Phys.* **15**, 5443–5471 (2013).

36. Chen, D. *Characterization and Control of Non-stoichiometry in Pr$_{0.1}$Ce$_{0.9}$O$_{2-\delta}$ Thin Films: Correlation with SOFC Electrode Performance.* PhD Thesis, Massachusetts Institute of Technology (2014).

37. Zhao, L., Perry, N. H., Daio, T., Sasaki, K. & Bishop, S. R. Improving the Si impurity tolerance of Pr$_{0.1}$Ce$_{0.9}$O$_{2-\delta}$ SOFC electrodes with reactive surface additives. *Chem. Mater.* **27**, 3065–3070 (2015).

38. Simons, P., Ji, H. Il, Davenport, T. C. & Haile, S. M. A piezomicrobalance system for high-temperature mass relaxation characterization of metal oxides: a case study of Pr-doped ceria. *J. Am. Ceram. Soc.* **100**, 1161–1171 (2017).

39. Riess, I. Characterization of solid oxide fuel cells based on solid electrolytes or mixed ionic electronic conductors. *Solid State Ion.* **90**, 91–104 (2003).

40. Adler, S. B. Reference electrode placement in thin solid electrolytes. *J. Electrochem. Soc.* **149**, E166–E172 (2002).

41. Thole, B. T. et al. 3*d* X-ray-absorption lines and the $3d^94f^{n+1}$ multiplets of the lanthanides. *Phys. Rev. B* **32**, 5107–5118 (1985).

42. Karnatak, R. et al. X-ray absorption studies of CeO$_2$, PrO$_2$, and TbO$_2$. I. Manifestation of localized and extended *f* states in the 3*d* absorption spectra. *Phys. Rev. B* **36**, 1745–1749 (1987).

43. Lu, Q. et al. Surface defect chemistry and electronic structure of Pr$_{0.1}$Ce$_{0.9}$O$_{2-\delta}$ revealed in operando. *Chem. Mater.* **30**, 2600–2606 (2018).

44. Chueh, W. C. & Haile, S. M. Electrochemistry of mixed oxygen ion and electron conducting electrodes in solid electrolyte cells. *Annu. Rev. Chem. Biomol. Eng.* **3**, 313–341 (2012).

45. Feng, Z. A. et al. Origin of overpotential-dependent surface dipole at CeO$_{2-x}$/gas interface during electrochemical oxygen insertion reactions. *Chem. Mater.* **28**, 6233–6242 (2016).

46. Nenning, A. et al. Ambient pressure XPS study of mixed conducting perovskite-type SOFC cathode and anode materials under well-defined electrochemical polarization. *J. Phys. Chem. C* **120**, 1461–1471 (2016).

47. Siegbahn, H. & Lundholm, M. A method of depressing gaseous-phase electron lines in liquid-phase ESCA spectra. *J. Electron Spectrosc. Relat. Phenom.* **28**, 135–138 (1982).

48. Guan, Z. *Probing and Tuning Far-from-Equilibrium Oxygen Exchange Kinetics on Electrochemical Solid-Gas Interfaces.* PhD thesis, Stanford Univ. (2018).

49. Schaube, M., Merkle, R. & Maier, J. Oxygen exchange kinetics on systematically doped ceria: a pulsed isotope exchange study. *J. Mater. Chem. A* **7**, 21854–21866 (2019).

50. Tsvetkov, N., Lu, Q., Sun, L., Crumlin, E. J. & Yildiz, B. Improved chemical and electrochemical stability of perovskite oxides with less reducible cations at the surface. *Nat. Mater.* **15**, 1010–1016 (2016).

51. Feng, Za, El Gabaly, F., Ye, X., Shen, Z.-X. & Chueh, W. C. Fast vacancy-mediated oxygen ion incorporation across the ceria–gas electrochemical interface. *Nat. Commun.* **5**, 4374 (2014).

52. Mueller, D. N., Machala, M. L., Bluhm, H. & Chueh, W. C. Redox activity of surface oxygen anions in oxygen-deficient perovskite oxides during electrochemical reactions. *Nat. Commun.* **6**, 6097 (2015).

53. Frank Ogletree, D., Bluhm, H., Hebenstreit, E. D. & Salmeron, M. Photoelectron spectroscopy under ambient pressure and temperature conditions. *Nucl. Instrum. Methods Phys. Res. A* **601**, 151–160 (2009).

54. Whaley, J. A. et al. Note: fixture for characterizing electrochemical devices in-operando in traditional vacuum systems. *Rev. Sci. Instrum.* **81**, 086104 (2010).

Author contributions

D.C. designed the experiment. Z.G. derived the general microkinetic model for MIECs and D.C. adapted the model for this study. D.C., Z.G. and D.Z. performed the experiments. S.N., L.T., E.C. and H.B. supported the beamline experiments. D.C. analysed the data. D.C., H.L.T. and W.C.C. wrote the manuscript. All authors revised the manuscript. W.C.C. supervised the project.

Competing interests

The authors declare no competing interests.

Additional information

Supplementary information is available for this paper at https://doi.org/10.1038/s41929-019-0401-9.

Correspondence and requests for materials should be addressed to W.C.C.

Reprints and permissions information is available at www.nature.com/reprints.

Publisher's note Springer Nature remains neutral with regard to jurisdictional claims in published maps and institutional affiliations.